COMMUNICATIONS IN COMPUTATIONAL PHYSICS
Vol. **4**, No. 1, pp. 72-101

Commun. Comput. Phys.
July 2008

Phase-Field Models for Biofilms II. 2-D Numerical Simulations of Biofilm-Flow Interaction

Tianyu Zhang[1], Nick Cogan[1] and Qi Wang[1,2,*]

[1] *Department of Mathematics, Florida State University, Tallahassee, FL 32306-4510, USA.*
[2] *School of Mathematics, Nankai University, Tianjin 300071, China.*

Received 10 September 2007; Accepted (in revised version) 20 October 2007

Available online 27 February 2008

Abstract. We study the biofilm-flow interaction resulting in biofilm growth, deformation and detachment phenomena in a cavity and shear flow using the phase field model developed recently [28]. The growth of the biofilm and the biofilm-flow interaction in various flow and geometries are simulated using an extended Newtonian constitutive model for the biofilm mixture in 2-D. The model predicts growth patterns consistent with experimental findings with randomly distributed initial biofilm colonies. Shear induced deformation, and detachment in biofilms is simulated in a shear cell. Rippling, streaming, and ultimate detachment phenomena in biofilms are demonstrated in the simulations, respectively, in a shear cell. Possible merging of detached biofilm blobs in oscillatory shear is observed in simulations as well. Detachment due to the density variation is also investigated shedding light on the possible bacteria induced detachment.

AMS subject classifications: 65M06, 76D05, 76A05, 76T30, 76Z05, 92C05
Key words: Biofilm, Cahn-Hilliard equation, phase filed, finite difference method, multiphase flow.

1 Introduction

Biofilms are ubiquitous in nature and manmade materials. Biofilms form when bacteria adhere to surfaces in moist environments by excreting a slimy, glue-like substance. Sites for biofilm formation include all kinds of surfaces: natural materials above and below ground, metals, plastics, medical implant materials, plants and body tissues. Wherever you find a combination of moisture, nutrients and a surface, you are likely to find biofilms [8, 14, 16, 20].

A biofilm community can be formed by a single bacterial species, but in nature biofilms almost always consist of rich mixtures of many species of bacteria, as well as fungi, algae,

*Corresponding author. *Email addresses:* zhang@math.fsu.edu (T. Zhang), cogan@math.fsu.edu (N. Cogan), wang@math.fsu.edu (Q. Wang)

yeasts, protozoa, other microorganisms, debris and corrosion products. Biofilms are held together by sugary molecular strands, collectively termed "extracellular polymeric substances" or "EPS". The cells produce EPS and are held together by these strands, allowing them to develop complex, three-dimensional, resilient, attached communities. Biofilms cost the U.S. literally billions of dollars every year in energy losses, equipment damage, product contamination and medical infections. But biofilms also offer huge potential for bio-remediating hazardous waste sites, bio-filtering municipal and industrial water and waste water, forming bio-barriers to protect soil and ground water from contamination, as well as heap leaching.

It is a challenge to model the live microorganism in biofilms and their transient growth and transport behavior. There have been various multi-fluid models proposed to predict growth behavior of biofilms [1,7,19,27] and models to simulate biofilm growth and transport phenomena [9, 17, 18, 22–25]. However, it becomes tricky when one uses the multi-fluid models to study biofilm dynamics in another fluid since the velocity boundary conditions for the multi-fluid model are often hard to define. When constitutive equations are also present for viscoelastic components, there could also be boundary conditions for the extra elastic stress tensor corresponding to the components, creating another layer of complications for the use of the models. Hence, for flow-biofilm interaction, a single fluid model would be more appropriate and efficient, in which a single mass average velocity serves as the measurable macroscopic velocity.

Recently, we developed a phase-field based hydrodynamic theory for mixtures of biofilm and solvent using the one fluid multi-component formulation [2, 28]. The model captures the long wave growth phenomenon exhibited in the biofilm growth. The preliminary study on 1-D biofilm growth shows promising results for the theory to be used in studying dynamics of the biofilm and the interaction with the ambient solvent. In this paper, we continue our investigation of the biofilm dynamics in 2 space dimensions using the phase field theory with an extended Newtonian constitutive equation for the EPS polymer network in the biofilm.

2 Mathematical model

We first recall the mathematical model developed for the mixture of biofilms and solvent in [28]. Let $\mathbf{v}$ be the average velocity, p the pressure, ϕ_n and ϕ_s the volume fraction of the polymer network and solvent respectively, and c the nutrient concentration. The phase field theory for biofilms consists of four sets of equations of multiple variations.

2.1 Momentum and continuity equation

Consider

$$\begin{aligned} &\nabla\cdot\mathbf{v}=0,\\ &\rho\frac{d\mathbf{v}}{dt}=\nabla\cdot(\phi_n\tau_n+\phi_s\tau_s)-[\nabla p+\gamma_1 kT\nabla\cdot(\nabla\phi_n\nabla\phi_n)], \end{aligned} \tag{2.1}$$

where $\rho=\phi_n\rho_n+\phi_s\rho_s$ is the effective density for the mixture, ρ_n and ρ_s are the density for the polymer network and the solvent, respectively, τ_n and τ_s are the extra stress tensor for the polymer network and the solvent, respectively, k is the Boltzmann constant, T is the temperature, γ_1 is a parameter measures the strength of the conformation entropy and γ_2 is the strength of the bulk free energy in the extended Flory-Huggin's mixing free energy density defined by [11, 12]

$$f=\frac{\gamma_1}{2}kT\|\nabla\phi_n\|^2+\gamma_2 kT\left[\frac{\phi_n}{N}\ln\phi_n+(1-\phi_n)\ln(1-\phi_n)+\chi\phi_n(1-\phi_n)\right]. \tag{2.2}$$

Here γ_2 is proportional to the reciprocal of the volume of the solvent molecule, N is the polymerization index for the polymer strand in the EPS network and χ is the mixing parameter. We note that the incompressibility condition implies

$$\phi_s+\phi_n=1. \tag{2.3}$$

2.2 Transport equation for nutrient substrates

Consider

$$\begin{aligned}&\frac{\partial}{\partial t}(\phi_s c)+\nabla\cdot(c\mathbf{v}\phi_s-D_s\phi_s\nabla c)=-g_c, \qquad \text{CA-model},\\ &\frac{\partial}{\partial t}(\phi_s c)+\nabla\cdot(c\mathbf{v}_s\phi_s-D_s\phi_s\nabla c)=-g_c, \qquad \text{CN-model},\end{aligned} \tag{2.4}$$

where c is the nutrient concentration and the nutrient consumption rate is given by

$$g_c=\phi_n Ac, \tag{2.5}$$

A is a constant and D_s is the diffusion constant for the nutrient substrate. The suffix A and N in CA and CN indicate either the average ($\mathbf{v}$) or the solvent ($\mathbf{v}_s$ defined below) velocity is used in the transport equations.

2.3 Transport equation for the volume fraction of the polymer network

Consider

$$\frac{\partial\phi_n}{\partial t}+\nabla\cdot(\phi_n\mathbf{v})=\nabla\cdot\left[\lambda\phi_n\nabla\frac{\delta f}{\delta\phi_n}\right]+g_n, \qquad \text{MCH-model}, \tag{2.6}$$

where λ is the mobility parameter and the polymer network production rate is given by

$$g_n=\epsilon\mu\phi_n\frac{c}{K_c+c}, \tag{2.7}$$

μ is the maximum production rate, K_c is the half-saturation constant and ϵ is a scaling parameter. The prefix M indicates the transport equation is a modified or singular Cahn-Hilliard equation with a polymer volume fraction dependent mobility [4, 5, 21, 26].

2.4 Constitutive equations

Consider

$$\begin{aligned}
&\tau_n = 2\eta_n \mathbf{D}, \tau_s = 2\eta_s \mathbf{D}, \qquad \text{VA-model}\\
&\tau_n = 2\eta_n \mathbf{D}_n, \tau_s = 2\eta_s \mathbf{D}_s, \qquad \text{VN-model}\\
&\frac{\partial \tau_n}{\partial t} + \mathbf{v}\cdot\nabla\tau_n - \mathbf{W}\cdot\tau_n + \tau_n\cdot\mathbf{W} - a[\mathbf{D}\cdot\tau_n + \tau_n\cdot\mathbf{D}]\\
&\qquad + \frac{\tau_n}{\lambda_1} = \frac{2\eta_n}{\lambda_1}\mathbf{D}, \quad \tau_s = 2\eta_s\mathbf{D}, \qquad \text{JSA-model}\\
&\frac{\partial \tau_n}{\partial t} + \mathbf{v}_n\cdot\nabla\tau_n - \mathbf{W}_n\cdot\tau_n + \tau_n\cdot\mathbf{W}_n - a[\mathbf{D}_n\cdot\tau_n + \tau_n\cdot\mathbf{D}_n]\\
&\qquad + \frac{\tau_n}{\lambda_1} = \frac{2\eta_n}{\lambda_1}\mathbf{D}_n, \quad \tau_s = 2\eta_s\mathbf{D}_s, \qquad \text{JSN-model}
\end{aligned} \tag{2.8}$$

where η_n and η_s are the viscosity for the polymer network and the solvent respectively. We note that the infinite relaxation time limit $\lambda_1 \to \infty$ and $\eta_n/\lambda_1 \to$ const yields the pure elastic theory while $\lambda_1 \to 0$ gives rise to the viscous limit [3, 10, 15]. The suffix A and N in the above equations indicate that either the average or network velocity is used in convection, respectively, where the polymer network velocity is defined by

$$\mathbf{v}_n = \mathbf{v} - \lambda\nabla\frac{\delta f}{\delta\phi_n}. \tag{2.9}$$

The solvent velocity is defined by

$$\mathbf{v}_s = \mathbf{v} + \frac{\lambda\phi_n}{\phi_s}\nabla\frac{\delta f}{\delta\phi_n}. \tag{2.10}$$

The rate of strain tensor and the vorticity tensor with respect to the average velocity are given by

$$\mathbf{D} = \frac{1}{2}[\nabla\mathbf{v} + \nabla\mathbf{v}^T], \quad \mathbf{W} = \frac{1}{2}[\nabla\mathbf{v} - \nabla\mathbf{v}^T].$$

The corresponding ones with respect to the network velocity are defined analogously

$$\mathbf{D}_n = \frac{1}{2}[\nabla\mathbf{v}_n + \nabla\mathbf{v}_n^T], \quad \mathbf{W}_n = \frac{1}{2}[\nabla\mathbf{v}_n - \nabla\mathbf{v}_n^T].$$

We investigate the dynamics of the biofilm in 2 space dimensions: $(x,y) \in \Omega = [0,L] \times [0,H]$, where H and L are positive constants. For the cavity geometry, we impose boundary conditions as follows on the boundary $\partial\Omega$.

$$\begin{aligned}
&[c\mathbf{v}\phi_s - D_s\phi_s\nabla c]\cdot\mathbf{n}|_{\partial\Omega} = 0, \quad \nabla\phi_n\cdot\mathbf{n}|_{\partial\Omega} = 0,\\
&[\mathbf{v}\phi_n - \Lambda\phi_n\nabla\frac{\delta f}{\delta\phi_n}]\cdot\mathbf{n}|_{\partial\Omega} = 0, \quad \mathbf{v}|_{\partial\Omega} = 0,
\end{aligned} \tag{2.11}$$

in which the first and the third boundary condition indicate vanishing normal fluxes for the nutrient flow and the polymeric flow, respectively. In some simulations, we impose a feeding condition,

$$c|_{y=H}=c^*,$$

at the top of the domain $y=H$. A moving top is also possible, where a prescribed boundary condition for the velocity is given to simulate shear flows. For shear flows, we impose periodic boundary conditions in x direction and the following physical ones in y direction: no-flux boundary conditions for the volume fraction of polymer network and nutrient substrate concentration, Dirichelet boundary condition for the velocity:

$$\begin{aligned}&[c\mathbf{v}\phi_s-D_s\phi_s\nabla c]\cdot\mathbf{n}|_{y=0,H}=0,\quad \nabla\phi_n\cdot\mathbf{n}|_{y=0,H}=0,\\&[\mathbf{v}\phi_n-\Lambda\phi_n\nabla\frac{\delta f}{\delta\phi_n}]\cdot\mathbf{n}|_{y=0,H}=0,\quad \mathbf{v}|_{y=0}=0,\mathbf{v}|_{y=H}=\mathbf{v}_0.\end{aligned}\tag{2.12}$$

Again the top feeding boundary condition could be given for c at $y=H$: $c|_{y=H}=c^*$.

3 Nondimensionalization

We use a characteristic time scale t_0 and length scale h to nondimensionalize the variables

$$\tilde{t}=\frac{t}{t_0},\quad \tilde{\mathbf{x}}=\frac{\mathbf{x}}{h},\quad \tilde{\mathbf{v}}=\frac{\mathbf{v}t_0}{h},\quad \tilde{p}=\frac{pt_0^2}{\rho_0h^2},\quad \tilde{c}=\frac{c}{c_0},\tag{3.1}$$

where c_0 is a characteristic nutrient substrate concentration. The length scale h is determined by the computational geometry while the time scale is done by either the growth time scale of the biofilm or the flow induced time scale. The following dimensionless equations arise

$$\begin{aligned}&\Lambda=\frac{\lambda\rho_0}{t_0},\quad \Gamma_1=\frac{\gamma_1kTt_0^2}{\rho_0h^4},\quad \Gamma_2=\frac{\gamma_2kTt_0^2}{\rho_0h^2},\\&Re_s=\frac{\rho_0h^2}{\eta_st_0},\quad Re_n=\frac{\rho_0h^2}{\eta_nt_0},\quad \tilde{D}_s=\frac{D_st_0}{h^2},\\&\tilde{\rho}=\phi_s\frac{\rho_s}{\rho_0}+\phi_n\frac{\rho_n}{\rho_0},\quad \tilde{A}=At_0,\quad \tilde{\mu}=\mu t_0,\quad \tilde{K}_c=\frac{K_c}{c_0},\end{aligned}\tag{3.2}$$

where Re_s and Re_n are the Reynolds number for the solvent and the polymer respectively, ρ_0 is an averaged density. In this paper, we use the extended Newtonian model for the polymeric stress tensor. For simplicity, we drop the ˜ on the dimensionless variables and the parameters and the system of governing equations for the biofilm in these

dimensionless variables are given by

$$\begin{aligned}
&\nabla\cdot\mathbf{v}=0,\\
&\rho\frac{d\mathbf{v}}{dt}=\nabla\cdot(\phi_n\tau_n+\phi_s\tau_s)-[\nabla p+\Gamma_1\nabla\cdot(\nabla\phi_n\nabla\phi_n)],\\
&\frac{\partial}{\partial t}(\phi_s c)+\nabla\cdot(c\mathbf{v}\phi_s-D_s\phi_s\nabla c)=-g_c,\\
&\frac{\partial\phi_n}{\partial t}+\nabla\cdot(\phi_n\mathbf{v})=\nabla\cdot(\Lambda\phi_n\nabla\frac{\delta f}{\delta\phi_n})+g_n.
\end{aligned}\tag{3.3}$$

where

$$\begin{aligned}
&\tau_n=\frac{2}{Re_n}\mathbf{D},\quad \tau_s=\frac{2}{Re_s}\mathbf{D},\quad g_c=A\phi_n c,\\
&g_n=\epsilon\mu\phi_n\frac{c}{K_c+c}.
\end{aligned}\tag{3.4}$$

The dimensionless mixing free energy density is now given by

$$f=\frac{\Gamma_1}{2}\|\nabla\phi_n\|^2+\Gamma_2\left[\frac{\phi_n}{N}\ln\phi_n+(1-\phi_n)\ln(1-\phi_n)+\chi\phi_n(1-\phi_n)\right].\tag{3.5}$$

Analogously, the other dimensionless equations can be obtained. To save space, we will not enumerate them here.

4 Numerical schemes

We use the finite difference method to solve the coupled flow, phase field equation, and nutrient concentration transport equation. We solve the coupled momentum transport equation and the continuity equation using a velocity corrected projection scheme developed by Guermond et al. [13]. We denote

$$\mathbf{R}=-\nabla\cdot(\Gamma_1\nabla\phi_n\nabla\phi_n)+\nabla\cdot(\phi_n\tau_n+\phi_s\tau_s-\frac{2}{Re_a}\mathbf{D}),\tag{4.1}$$

where Re_a is an averaged Reynolds number. The momentum transport equation is rewritten as

$$\rho(\frac{\partial}{\partial t}\mathbf{v}+\mathbf{v}\cdot\nabla\mathbf{v})=-\nabla p+\frac{1}{Re_a}\nabla^2\mathbf{v}+\mathbf{R}.\tag{4.2}$$

We calculate $\mathbf{v}$ and the pressure in three steps. We present the scheme for the case of periodic boundary conditions in the x direction and physical one in the y direction in the following. For simplicity, the second order extrapolation in time of any function f is denoted by $\overline{f}^{n+1}=2f^n-f^{n-1}$.

Step 1:

$$\begin{cases} \rho^{n+1}[\frac{3\mathbf{u}^{n+1}-4\mathbf{v}^n+\mathbf{v}^{n-1}}{2\Delta t}]+\rho^{n+1}\overline{\mathbf{v}}^{n+1}\cdot\nabla\mathbf{u}^{n+1}+\nabla p^n+\frac{1}{Re_a}[\nabla s^n-\nabla^2\mathbf{u}^{n+1}]=\overline{\mathbf{R}}^{n+1}, \\ \mathbf{u}^{n+1}|_{y=0}=0,\mathbf{u}^{n+1}|_{y=H}=\mathbf{v}_0. \end{cases} \tag{4.3}$$

Step 2: We implement the projection step by solving a Poisson equation with the Neumann boundary condition:

$$\begin{cases} -\nabla\cdot(\frac{1}{\rho^{n+1}}\nabla\psi^{n+1})=\nabla\cdot\mathbf{u}^{n+1}, \\ \frac{\partial\psi^{n+1}}{\partial n}|_{y=0,H}=0. \end{cases} \tag{4.4}$$

Step 3: We correct the velocity, pressure and the auxiliary variable s.

$$\begin{cases} \mathbf{v}^{n+1}=\mathbf{u}^{n+1}+\frac{1}{\rho^{n+1}}\nabla\psi^{n+1}, \\ s^{n+1}=s^n-\nabla\cdot\mathbf{u}^{n+1}, \\ p^{n+1}=p^n-\frac{3\psi^{n+1}}{2\Delta t}+\frac{1}{Re_a}s^{n+1}. \end{cases} \tag{4.5}$$

Here $s^0=0$ and $\mathbf{v}^1,s^1,p^1,\phi_n^1,c^1$ are computed by a first order scheme.

The phase field equation for the polymer volume fraction ϕ_n is discretized by

$$\begin{aligned} &\frac{3\phi_n^{n+1}-4\phi_n^n+\phi_n^{n-1}}{2\Delta t}+\mathbf{v}^{n+1}\cdot\nabla\phi_n^{n+1} \\ &=g_n^{n+1}+\Lambda\nabla\cdot\overline{\phi_n}^{n+1}\nabla\Big(-\Gamma_1\nabla^2\phi_n^{n+1}-2\Gamma_2\chi\phi_n^{n+1}-\Gamma_2(-\frac{1}{N}\overline{\ln\phi_n}^{n+1}+\overline{\ln(1-\phi_n)}^{n+1})\Big). \end{aligned} \tag{4.6}$$

The substrate concentration transport equation is discretized by

$$\begin{aligned} &\frac{3\phi_s^{n+1}c^{n+1}-4\phi_s^nc^n+\phi_s^{n-1}c^{n-1}}{2\Delta t}+\mathbf{v}^{n+1}\cdot\nabla(c^{n+1}\phi_s^{n+1}) \\ &=g_c^{n+1}+\nabla\cdot(D_s\phi_s^{n+1}\nabla c^{n+1}). \end{aligned} \tag{4.7}$$

The spatial discretization is done using central differences to ensure at least second order accuracy in space. The boundary conditions at the top and the bottom boundary $y=1,0$ are handled in the following way.

We use uniform mesh size in both spatial and temporal discretization, where the time step size is Δt and spatial mesh size is $\Delta x=L/M_x,\Delta y=1/M_y$. The computational domain $\Omega=[0,L]\times[0,1]$ is divided into uniform cells by nodes $(x_i,y_j)=(i\Delta x,j\Delta y),i=0,\cdots,M_x,j=0,\cdots,M_y$. we denote the value of the numerical solution of (4.6) and (4.7) at $(n\Delta t,i\Delta x,j\Delta y)$ by $\phi_{n,i,j}^n$, $c_{i,j}^n$ respectively. For either the case of the cavity or the shear flow geometry, we have $\mathbf{v}\cdot\mathbf{n}|_{y=0,1}=0$. Thus, the boundary conditions for ϕ_n and c given by (2.12) becomes

$$\nabla c\cdot\mathbf{n}|_{y=0,1}=0,\quad \nabla\phi_n\cdot\mathbf{n}|_{y=0,1}=0,\quad \nabla\frac{\delta f}{\delta\phi_n}\cdot\mathbf{n}|_{y=0,1}=0. \tag{4.8}$$

The discrete forms of the boundary conditions (4.8) are given by

$$\begin{aligned}
&\phi^n_{n,i,1}=\phi^n_{n,i,-1}, \quad \phi^n_{n,i,2}=\phi^n_{n,i,-2},\\
&\phi^n_{n,i,M_y+1}=\phi^n_{n,i,M_y-1}, \quad \phi^n_{n,i,M_y+2}=\phi^n_{n,i,M_y-2},\\
&c^n_{i,1}=c^n_{i,-1}, \quad c^n_{i,M_y+1}=c_{i,M_y-1}, \quad i=0,\cdots,M_x.
\end{aligned} \tag{4.9}$$

The overall scheme is second order in space and time. To achieve second order accuracy in time, extrapolation is used for the **R** term in momentum transport equation (4.3) and the $\ln\phi_n$ and $\ln(1-\phi_n)$ terms in the phase filed equation (4.6). The density of solvent and polymer network are set to be the same, thus ρ^n is in fact a constant. The averaged Reynolds number Re_a is computed by

$$Re_a=\phi^n_{max}Re_n+(1-\phi^n_{max})Re_s,$$

where

$$\phi^n_{max}=\max\{\phi^n_{n,i,j},\ 0\le i\le M_x, 0\le j\le M_y\}.$$

Thus Re_a is a constant at each time step t_n, but varies with time. We run the mesh refinement test for $\Delta x=\Delta y=1/32,1/64,1/128$ respectively. The results show second order error reduction in both time and space. Thus our numerical scheme is convergent and stable upon mesh refinement. All numerical results presented here are for $\Delta x=\Delta y=1/64$ except in Fig. 1 where $\Delta x=\Delta y=1/128$ are used.

5 Numerical results

We study dynamics of the biofilm-solvent interaction in two representative 2-D flow geometries: a rectangular cavity where the velocity is zero at the boundaries or maybe nonzero at the top (mimicking a cavity in a well-established flow field) and a shear cell with the periodic boundary condition for all physical variables in the principal flow direction and the physical one in the transverse direction. The physical or shear boundary condition is divided into the case of steady and oscillatory transient conditions, respectively. The dimensionless parameter values in the simulations for the cavity case are set at

$$\begin{aligned}
&Re_s=9.98\times10^{-4}, \quad Re_n=2.33\times10^{-9}, \quad \Lambda=1\times10^{-10},\\
&\Gamma_1=33.467, \quad \Gamma_2=1.29\times10^{6}, \quad D_s=2.3,\\
&\mu=0.14, \quad K_c=0.15, \quad A=100.
\end{aligned}$$

For the weak shear flow, the polymer viscosity is reduced to $Re_n=2.33\times10^{-6}$ to achieve the detachment effect in the computational time scale. Table 1 lists the range of the dimensional parameter values used in our simulations.

In the simulations presented next, we first examine the growth of biofilms in a cavity and their dynamics while coupled with the solvent flow; then, we simulate the growth and detachment phenomena in a shear cell in both the weak and strong flow regimes.

Table 1: Parameter values used in the simulation.

Symbol	Parameter	value	Unit
T	Temperature	303	Kelvin
γ_1	Distortional energy	8×10^{6}	$\mathrm{kgm^{-1}s^{-2}}$
γ_2	Mixing free energy	3×10^{17}	$\mathrm{kgm^{2}s^{-2}}$
χ	Flory-Huggins parameter	0.6	
λ	Mobility parameter	1×10^{-10}	$\mathrm{kg^{-1}m^{3}s}$
N	Generalized polymerization parameter	1×10^{3}	
μ	Max. Production rate	1.4×10^{-4}	$\mathrm{kgm^{-3}s^{-1}}$
K_c	Half saturation constant	1.5×10^{-4}	$\mathrm{kgm^{-3}}$
A	Max. Consumption rate	0.1	$\mathrm{kgm^{-3}s^{-1}}$
D_s	Substrate diffusion coefficient	2.3×10^{-9}	$\mathrm{m^{2}s^{-1}}$
η_n	Dynamic viscosity of network	4.3×10^{2}	$\mathrm{kgm^{-1}s^{-1}}$
η_s	Dynamic viscosity of solvent	1.002×10^{-3}	$\mathrm{kgm^{-1}s^{-1}}$
ρ_n	Network density	1×10^{3}	$\mathrm{kgm^{-3}}$
ρ_s	Solvent density	1×10^{3}	$\mathrm{kgm^{-3}}$
c_0	Characteristic substrate concentration	1×10^{-3}	$\mathrm{kgm^{-3}}$
h	Characteristic length scale	1×10^{-3}	m
t_0	Characteristic time scale	1×10^{3}	s
L	x-direction size of Ω	1 or 4	
M_x	x-direction number of sub-intervals	64 or 256	
M_y	y-direction number of sub-intervals	64	

5.1 Growth of biofilms in a cavity

The 1-D study on the linearized stability of constant steady states can be extended to multidimensional cases trivially. We will refer readers to our work in part I on the detailed derivation of the 1-D case [28]. The stability analysis shows that a homogeneous biofilm is subject to a long wave instability leading to growth whenever the wave length of the 2-D biofilm colony exceeds a critical value.

In the 2-D simulation presented below, the no-flux boundary conditions are imposed for the polymer network volume fraction ϕ_n and the nutrient concentration c on all boundaries except that $c = c^\star$ is given at $y = 1$ (this is also known as the top feeding boundary condition). The velocities are assumed to be vanishing at all the boundaries when boundaries are fixed. This setup mimics a fixed container with nutrient being fed through the top boundary. For instance, a cavity in a large flow field where the velocity at the open end of the cavity is slow can be essentially approximated by this boundary condition.

We first consider the scenario in which the initial distribution of the biofilm is uniform except for a hump extruding into the solvent region shown in Fig. 1. The hump is located at the center of the biofilm-solvent interface and eventually grows to a mushroom shape

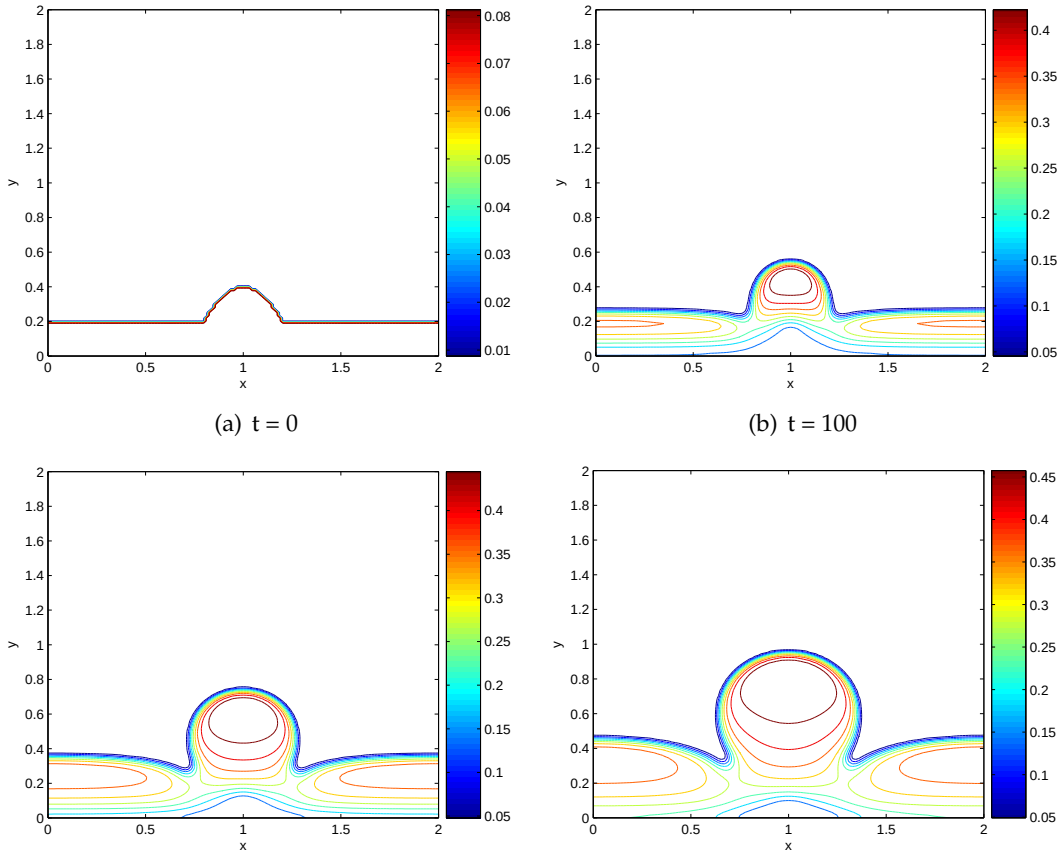

Figure 1: Growth of the biofilm with a single hump extruding into the solvent region in the initial profile in a cavity. A mushroom shaped growth is shown at a later time. The growth at the center sucks up some polymer network from interior to grow upward. The curves shown are level curves of ϕ_n. The biofilm solvent interface is defined by $\phi_n = 0$.

due to the accessibility to nutrients at the interface as well as in the interior. This pattern of growth is often observed in biofilm growth [6,7]. Here, our model captures it nicely. Fig. 1 plots the growth of the biofilm at a few selected time slots. We note that the characteristic time scale used in the simulation is $t_0 = 1000$ seconds, thus the dimensionless time $t = 300$ is approximately 3.5 days.

To explain the situation better, we also plot the contour of the polymer network velocity $\mathbf{v}_n$ given by (2.9) in Fig. 2(a) and the contour of the pressure in Fig. 2(b) at time $t = 200$. Fig. 2(a) clearly demonstrates the agreement of the growth of the biofilm with the velocity profile. Namely, the horizontal velocity u is positive on the right half of the mushroom shaped hump and negative on the left half while the vertical velocity v is positive on the network-solvent interface, demonstrating the spatial growth/expansion of biomass into the solvent region. If the excessive velocity $-\lambda\nabla\delta f/\delta\phi_n$ is denoted by $\mathbf{v}_e$,

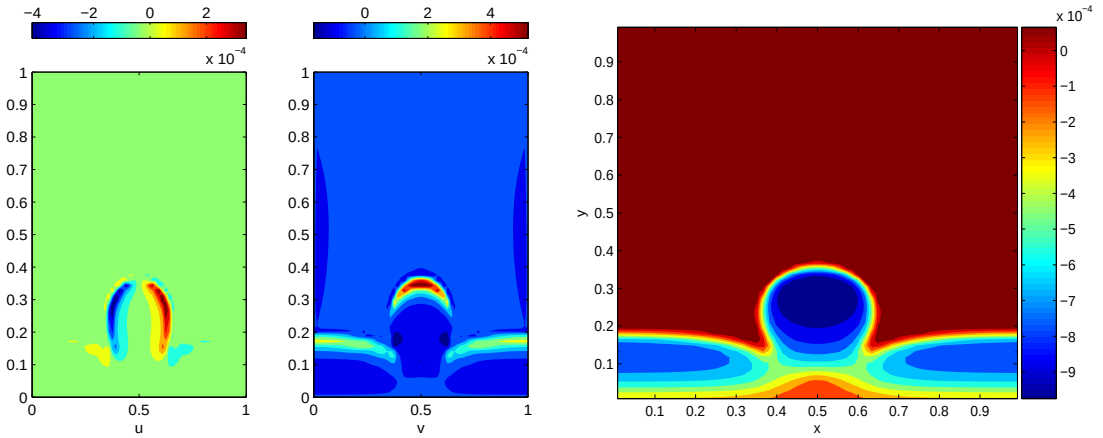

(a) Velocity (b) Pressure

Figure 2: Contour plot of the velocity and the pressure at $t=200$ for the biofilm with a single mushroom shaped growth pattern at the center. The velocity profile correlates with the growth direction and the pressure correlates inversely with the volume fraction, which explains the upward migration of the polymer network pulled behind the growing hump.

then (2.9) becomes

$$\mathbf{v}_n = \mathbf{v} + \mathbf{v}_e.$$

We observe that the magnitude of $\mathbf{v}_e$ is 10^{-4} while it is 10^{-5} for $\mathbf{v}$, thus the network velocity is indeed dominated by the excessive velocity induced by the gradient of chemical potential. In another word, the spatial expansion is fueled essentially by mixing! Fig. 2(b) shows that the pressure contour is very closely related to the polymer network profile. The pressure is almost constant in the pure solvent region and has the largest gradient at the network-solvent interface. In the interior of the mushroom region, the pressure drops leaving a low pressure core; it recovers near the bottom substrate right under the mushroom region. From the figures, we can see that the pressure correlates with the magnitude of the polymer volume fraction inversely: the lower is the pressure in the region, the higher the volume fraction is.

In a more general setting, we simulate the evolution of multiple humps in the initial distribution shown in Fig. 3, an analogous growth for each hump occurs nearly uniformly. It also shows that the top part of the mushroom grows faster due to its accessibility to the nutrient than its lateral region due to apparent topological constraints imposed by the neighboring mushrooms. We note that these results are similar to those obtained in [6] using a two-fluid derivation. We view these results as a validation of our model formulation.

Fig. 4 shows the growth of the biofilm with an initially flat interface between the biofilm and the solvent but with inhomogeneously distributed volume fraction values. It can be seen that the biofilm-solvent interface becomes inhomogeneous as the biofilm grows. This is because areas with higher network concentration has a larger network production rate, lower pressure, and thus grows faster. The polymer-network inhomo-

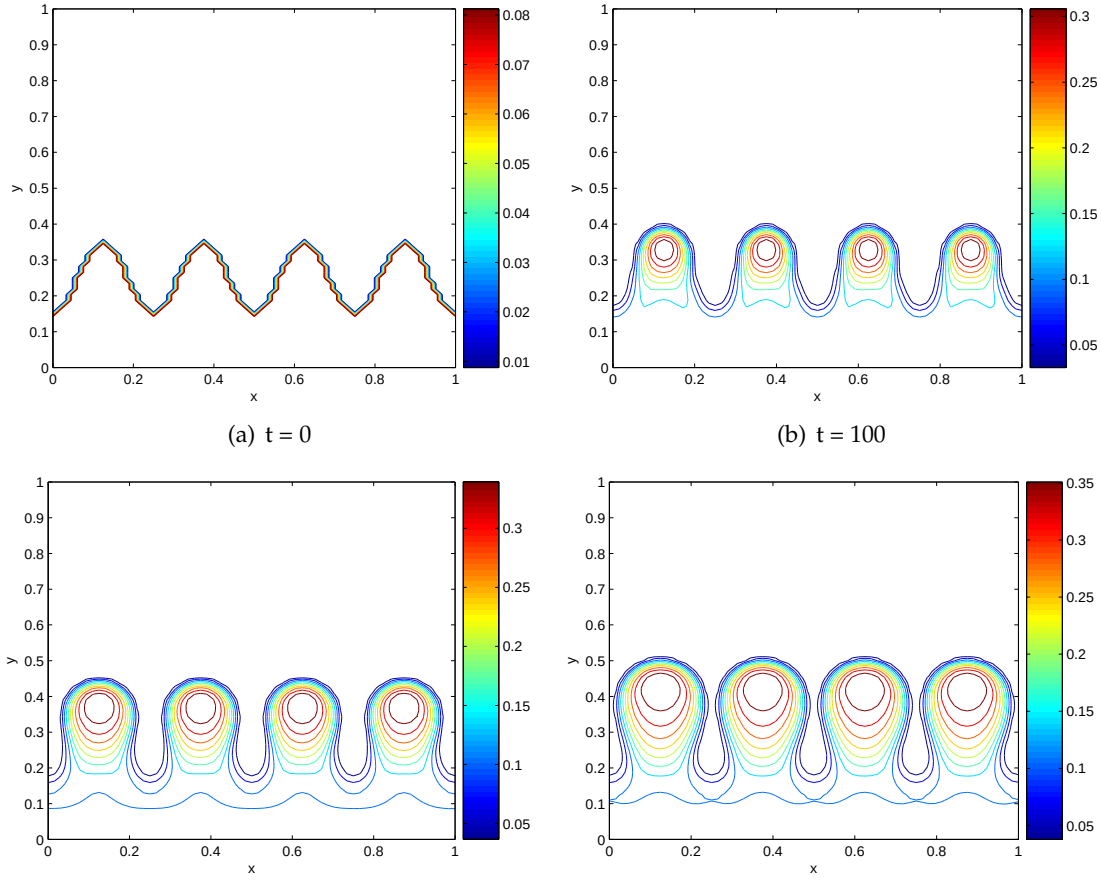

(a) t = 0 (b) t = 100

(c) t = 200 (d) t = 300

Figure 3: Growth of the biofilm with multiple humps at various time. An array of mushroom shaped growth is shown.

geneity induced growth can be linked to the biofilm colonies where the polymer volume fraction is inhomogeneous perhaps due to the presence of bacteria or solvent. Although the current model does not model the bacteria species explicitly, the simulation nonetheless reveals some growth features loosely related to inhomogeneity in the effective polymer network due to the presence of bacteria clusters.

When the biofilm is distributed as an inhomogeneously distributed array of colony islands, we simulate their respective growth. Fig. 5 is the contour plot of the polymer volume fraction ϕ_n of the randomly distributed biofilm colonies with variable initial volume fraction values. It shows that the initial volume fraction of the islands is not essential to the growth, but the distance from island to the top ($y=1$ where the nutrient is supplied) is more relevant to the growth. At the beginning of the growth process, all islands are growing since they all have access to the nutrient nearby. The colonies close to $y=1$ grow larger and consume large amount of the nutrient supplied from the top such that the nu-

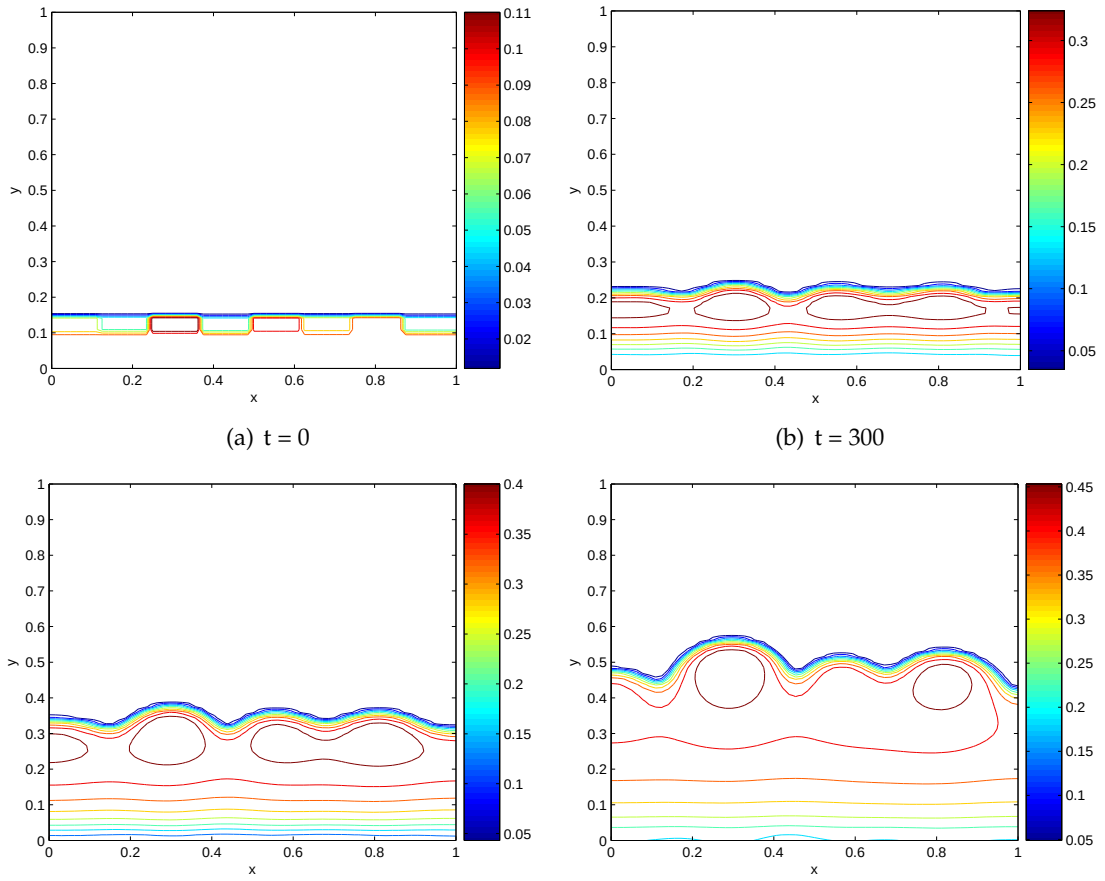

(a) t = 0 (b) t = 300

(c) t = 600 (d) t = 900

Figure 4: Growth of the flat-interface of an inhomogeneous biofilm. The volume fraction varies in space and higher concentrated areas bulges into the solvent region after the growth begins. The interface grows into the solvent region non-uniformly.

trient supply to the bottom is somehow hampered leading to reduced or even stopped growth of the islands at the bottom. Eventually the biofilm colonies expand to the top boundary where there are continuous supplies of the nutrient so that the biofilm grows exponentially. When this happens, the computation may eventually break down.

We next examine biofilm dynamics in a plane shear flow to investigate the detachment phenomena associated with the flow biofilm interaction.

5.2 Biofilm dynamics in shear flows

We investigate the biofilm flow interaction in shear in two distinct regimes: weak shear and strong shear. In order to contrast these two cases, we retain the growth characteristic time scale t_0. Then, the dimensionless driving speed of the shearing plate is signatured by small and large values, respectively.

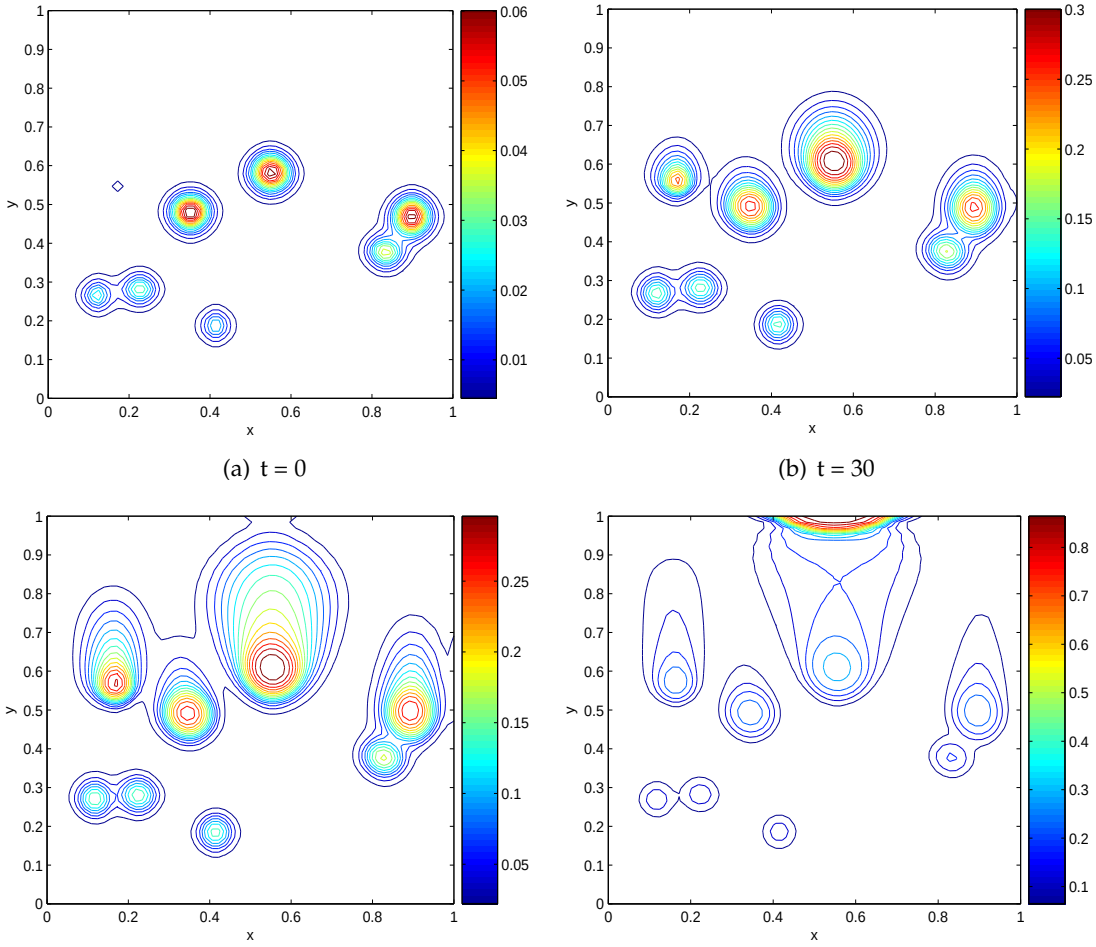

(a) t = 0 (b) t = 30

(c) t = 50 (d) t = 60

Figure 5: Growth of inhomogeneously distributed colony islands with variable volume fraction values. The contour plots of the polymer volume fraction ϕ_n showing the growth of randomly distributed colony islands. The biofilm colonies grows faster near the boundary where the nutrient is continuously fed.

5.2.1 Dynamics in weak shear

In this set of simulations, we adjust the viscosity of the biofilm to the lower end in order to capture the detachment phenomenon within a reasonable computational time frame since in the higher viscosity range, the biofilm is essentially too viscous to disintegrate in the time scale we simulate. Considering the inhomogeneity in the actual biofilm and the spatially distributed bacteria sites, it makes sense to use the lower viscosity value for the biofilm in the study. We first consider a computational cell of the same size in both x and y direction as in the previous cavity case. The boundary condition in x direction is periodic while it is physical in the y-direction. Fig. 6 shows the effect of shear flow

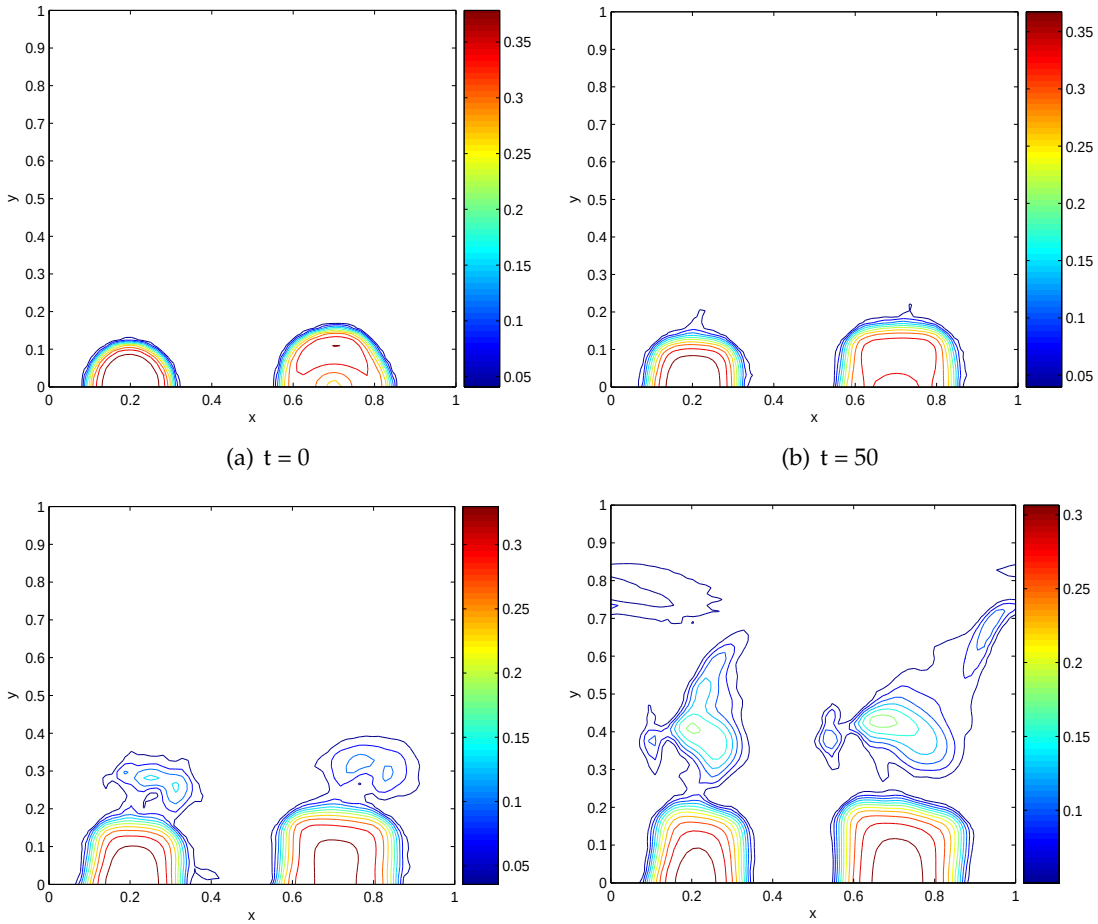

Figure 6: Shear flow over two humps with EPS production showing shedding effect. The driving velocity at $y=1$ is $u=0.1$.

generated by the moving plate on the top at the velocity

$$u|_{y=1}=0.1, \quad v|_{y=1}=0$$

over two humps of biofilm while the nutrient is continuously fed at the top. Since the size of the humps is large and interface between the biofilm and the solvent is smooth, we observe only small pieces of biofilm shed off or separate away from the bulk biofilm and then grow on their own. This simulation perhaps can be linked to the streaming phenomenon seen in the flow biofilm interaction.

We next look into the growth of two necked mushroom shaped humps with less volume fraction in the neck region. The interfacial deformation pattern changes. Instead of shedding off of smaller colonies, the large chunk of biofilm from the neck up is blown

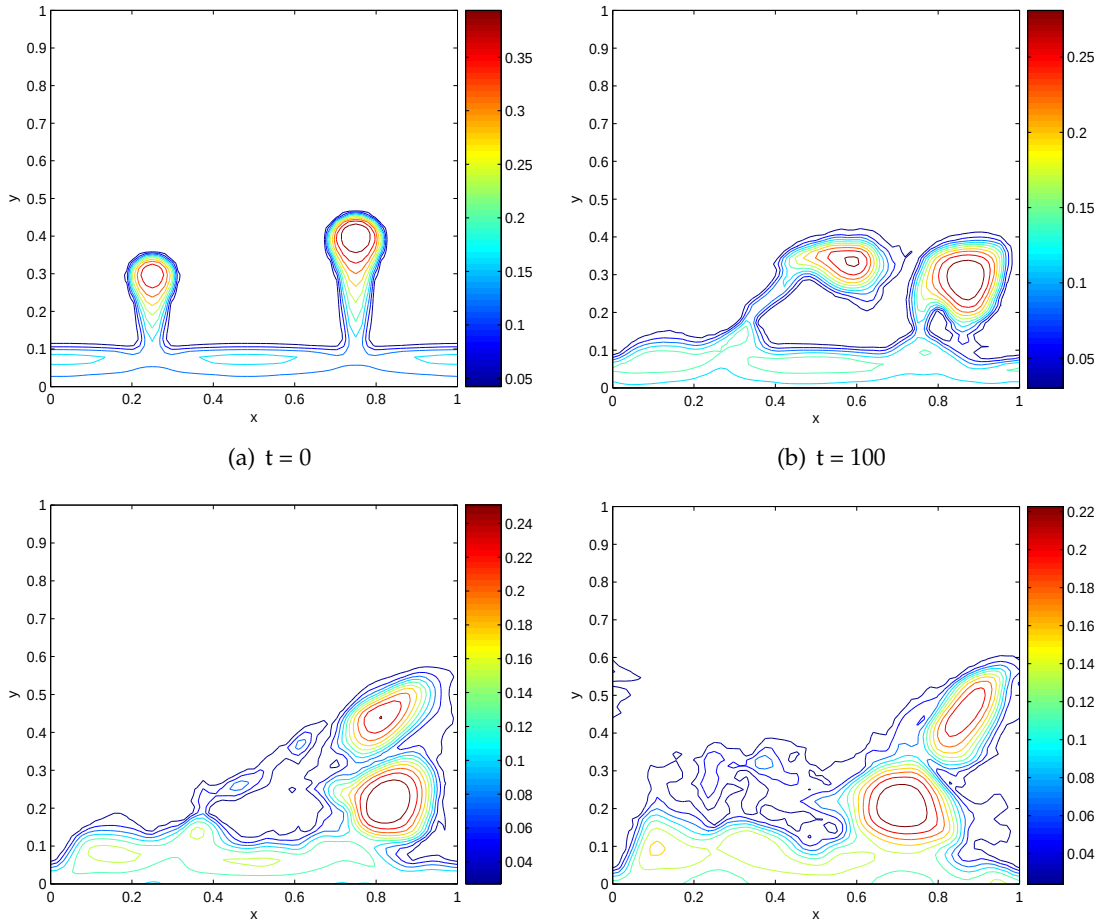

Figure 7: Shear flow over two mushroom shaped biofilm humps without EPS production showing pinching and detachment effect. The driving velocity at $y=1$ is $u=0.5$.

off. There is little shedding going on before the blob is completely blown off the base. Fig. 7 shows some snap shots of the deformation process and the break-off of the blob region above the neck. The smaller one with thinner neck is snapped away first. It then overtakes the larger mushroom biofilm blob downstream.

We next enlarge the computational domain of the shear cell to 4:1 in x vs y direction. We simulate the deformation of two peninsula shaped biofilm extrusions. They differ from the mushroom shaped in that the necks are now thicker than the heads. Fig. 8 shows the shear flow over the two peninsula on a flat base, where the value of ϕ_n at the thin end is around 0.11 (higher than the value at the base 0.09). The shear velocity at $y=1$ is $u=0.1, v=0$. We observe that these two humps are bent and stretched downstream due to the shear flow, but are not detached from the base in the simulation.

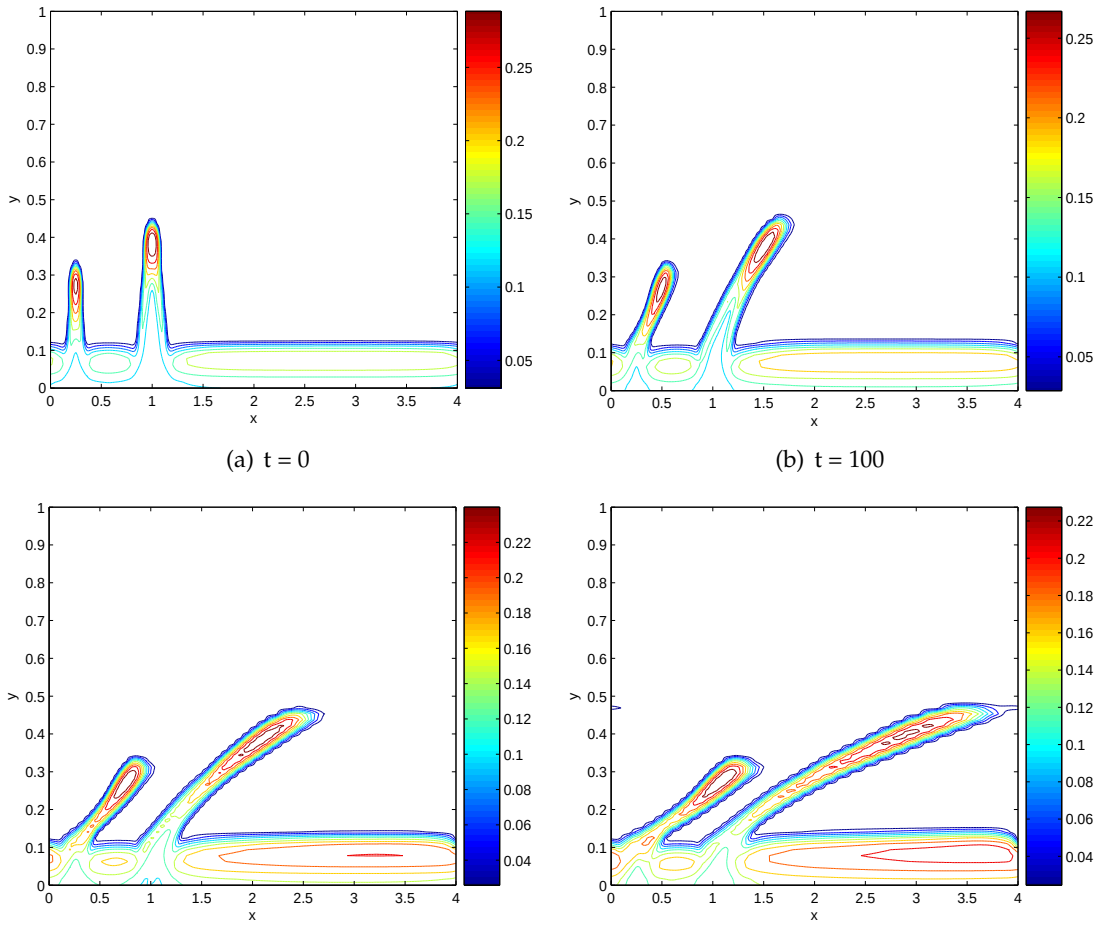

(a) t = 0 (b) t = 100

(c) t = 200 (d) t = 300

Figure 8: Shear flow over two peninsula shaped humps with EPS production showing bending effects in shear.

Fig. 9 depicts the shear flow over two mushroom shaped humps on a flat base, where the neck is thin and the value of ϕ_n at the neck is around 0.08 (lower than the value at the base 0.09). This mimics the situation where the bacteria are rich around the neck of the mushroom and the polymer eps volume fraction is low. Shear velocity at $y=1$ is $u=0.1, v=0$. We observe that these two humps are not only bent and stretched to the downstream direction by the shear flow, but also separated from the base eventually. We also note the second downstream hump pinches off in this simulation. (This is different from what we observe in the square domain $[0,1]\times[0,1]$ in that the two humps pinch off here equally easily, whereas the upstream one detaches more easily in the smaller square domain case.)

Fig. 10 portraits the shear flow over two smooth humps with $u|_{y=1}=0.5$. It clearly demonstrates the shedding effect on the downstream hump. It also shows that as time

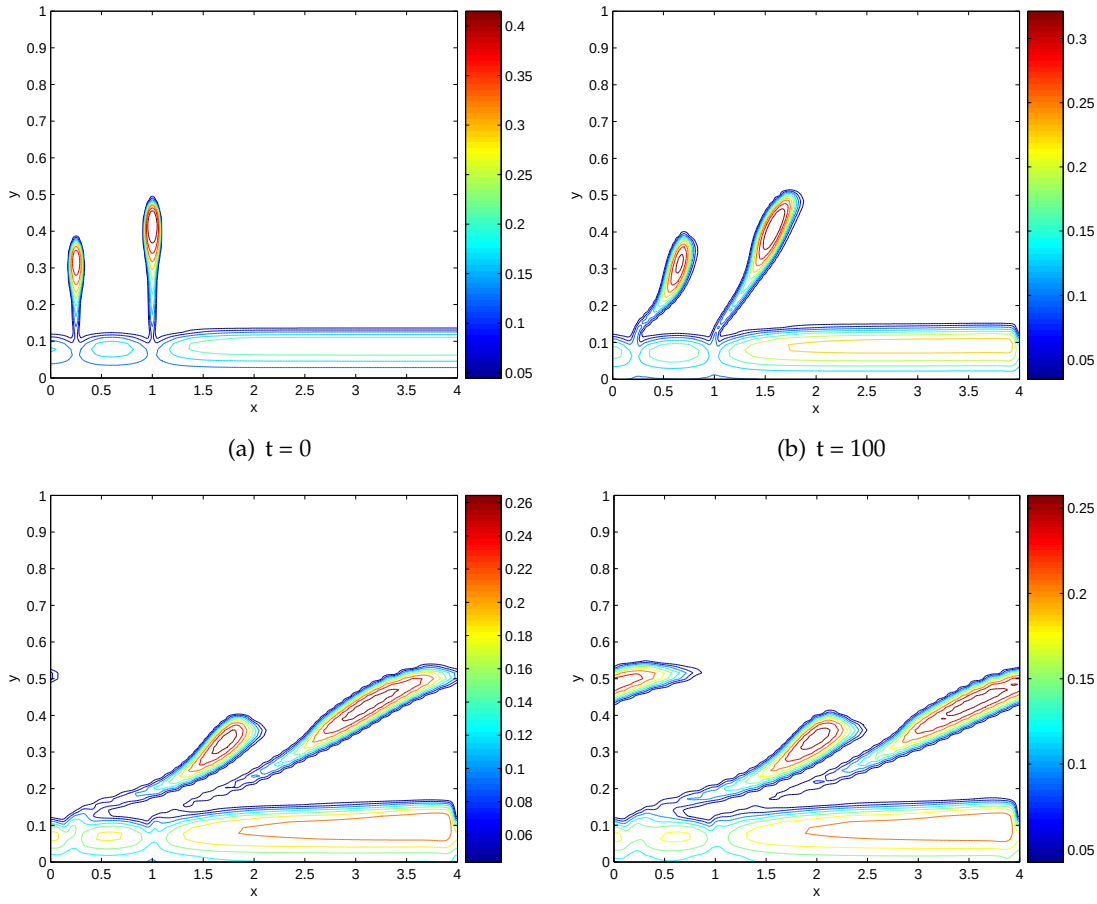

Figure 9: Shear flow over two mushroom shaped humps with thin necks while the EPS production is considered in the model. The mushroom shaped downstream hump detaches first.

goes by, the dispersed polymer islands grow and could split into even smaller pieces. Fig. 11 depicts the contour plot of the vorticity and the pressure in this simulation. We observe that at $t=50$ (before the shedding ensues), the maximum of the magnitude of the vorticity (all negative) appears at the top of the second hump (around $x=1.5, y=0.25$). This may explain why shedding takes place on the top of the second hump first, namely, shedding is caused by the larger vorticity of the flow and takes place at where the vorticity is the largest. Similarly, at $t=100$, the magnitude of the vorticity is large above the dispersed pieces of polymers to the right (around $x=3.5, y=0.28$), and we see at $t=125$, there is a small piece of polymer network splits off.

We also repeat the simulation without the EPS production. We notice that the shedding and detachment effect occurs slightly earlier when EPS production is not included. This indicates that the EPS production enhances or strengthens the polymer network and

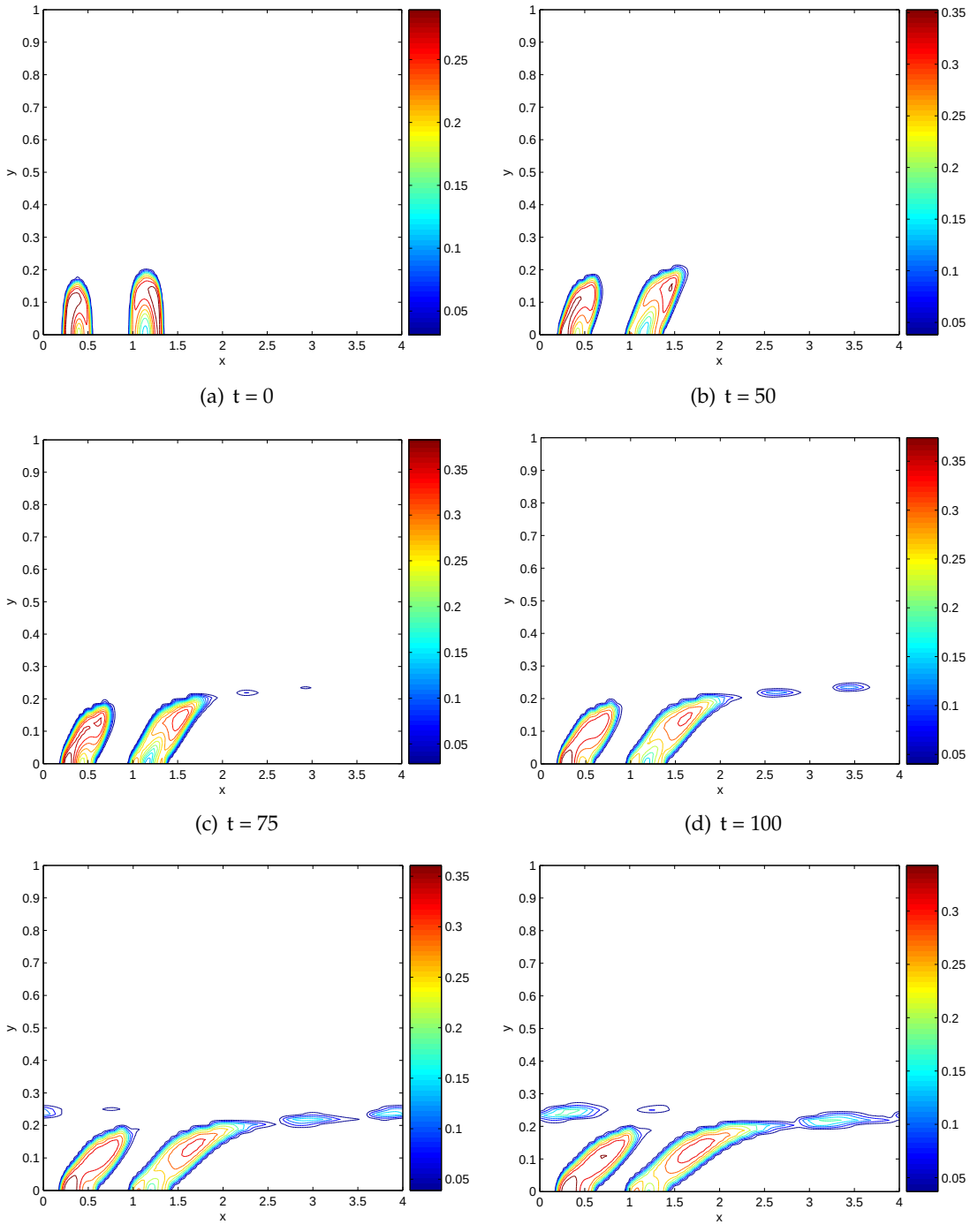

(a) t = 0 (b) t = 50

(c) t = 75 (d) t = 100

(e) t = 125 (f) t = 150

Figure 10: Shear flow over two humps with smooth interface while the EPS production is considered in the model. Shedding or streaming occurs from the top of the downstream hump.

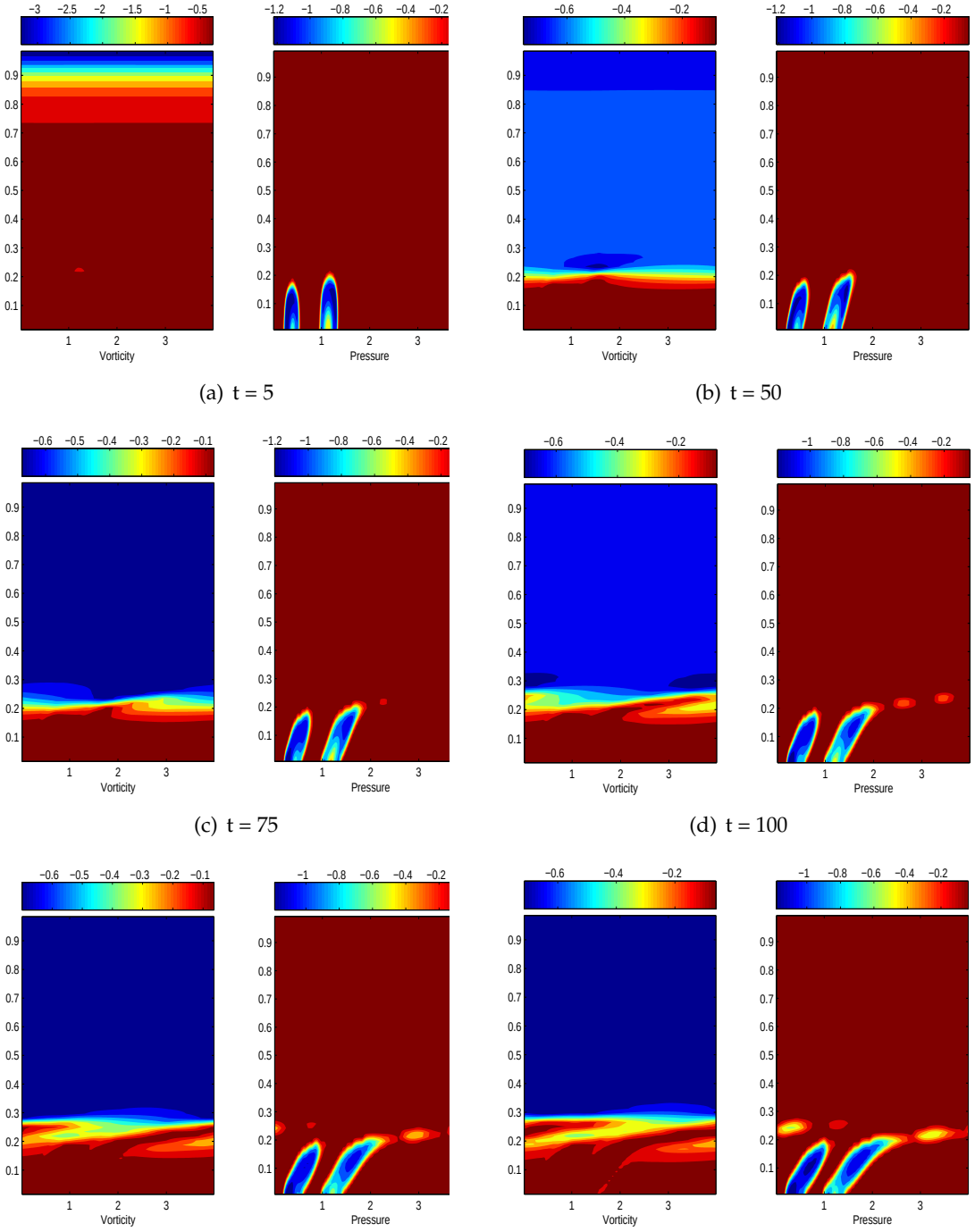

(a) t = 5 (b) t = 50

(c) t = 75 (d) t = 100

(e) t = 125 (f) t = 150

Figure 11: Contour plots of the vorticity and the pressure for shear flows over two humps with smooth interfaces while the EPS production is considered in the model.

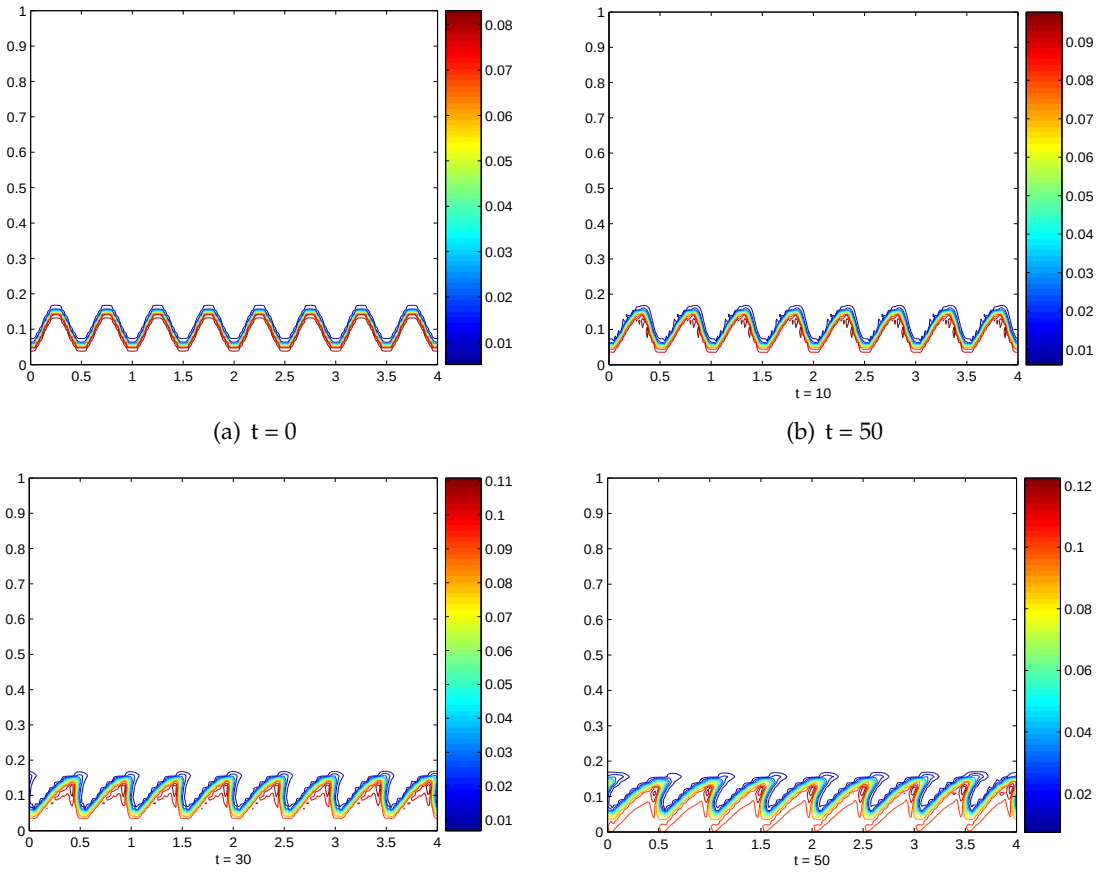

(a) t = 0 (b) t = 50

(c) t = 200 (d) t = 250

Figure 12: Rippling effect in shear flows over an array of low amplitude humps in biofilm-solvent interface while the EPS production is turned on. The driving velocity at $y=1$ is $u=1$.

tend to stabilize against the flow induced interfacial instability in the pinch-off and shedding scene.

Fig. 12 shows a simulation of the shear flow over an array of low amplitude humps while the EPS production is considered in the model, where the driving speed is set at $u|_{y=1}=1$. Due to their small amplitudes, the humps are skewed with their peaks tilting towards the flow direction demonstrating the rippling effect pattern in the biofilm by an ambient flow field. At a later time, some streaming is shown to emerge at the peaks of the ripples.

Next, we investigate the effect of an oscillatory shear on the biofilm-flow interaction. Fig. 13 shows the effect of an oscillatory shear flow with velocity

$$u=0.5\sin(\frac{2\pi}{100}t), \quad v=0 \quad \text{at } y=1$$

over the biofilm with two humps on a flat base. The EPS production is not considered

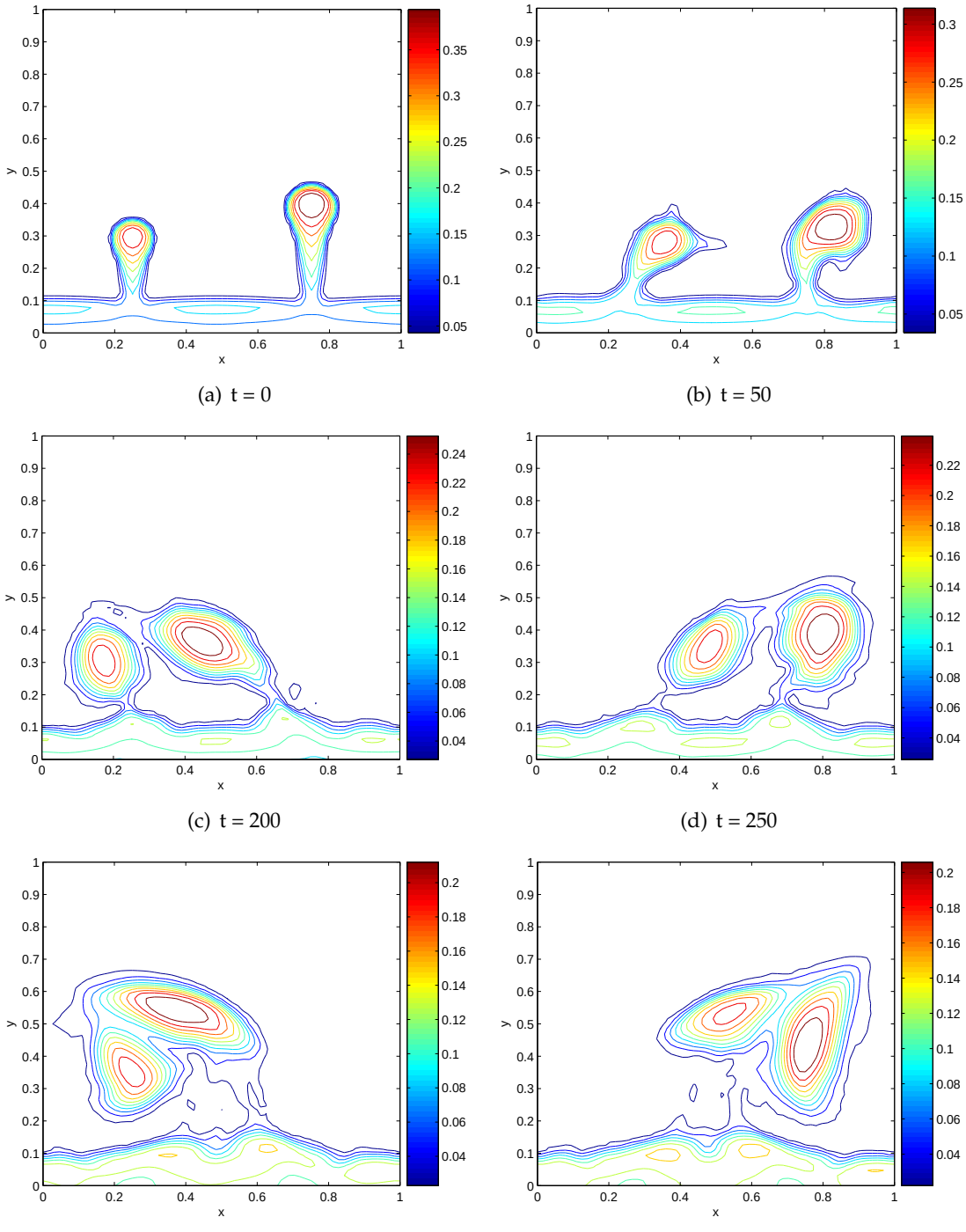

Figure 13: Oscillatory shear flow over two sturdy humps without EPS production, showing stronger pinching effect. Shear velocity at $y=1$ is $u=0.5\sin(\frac{2\pi}{100}t)$.

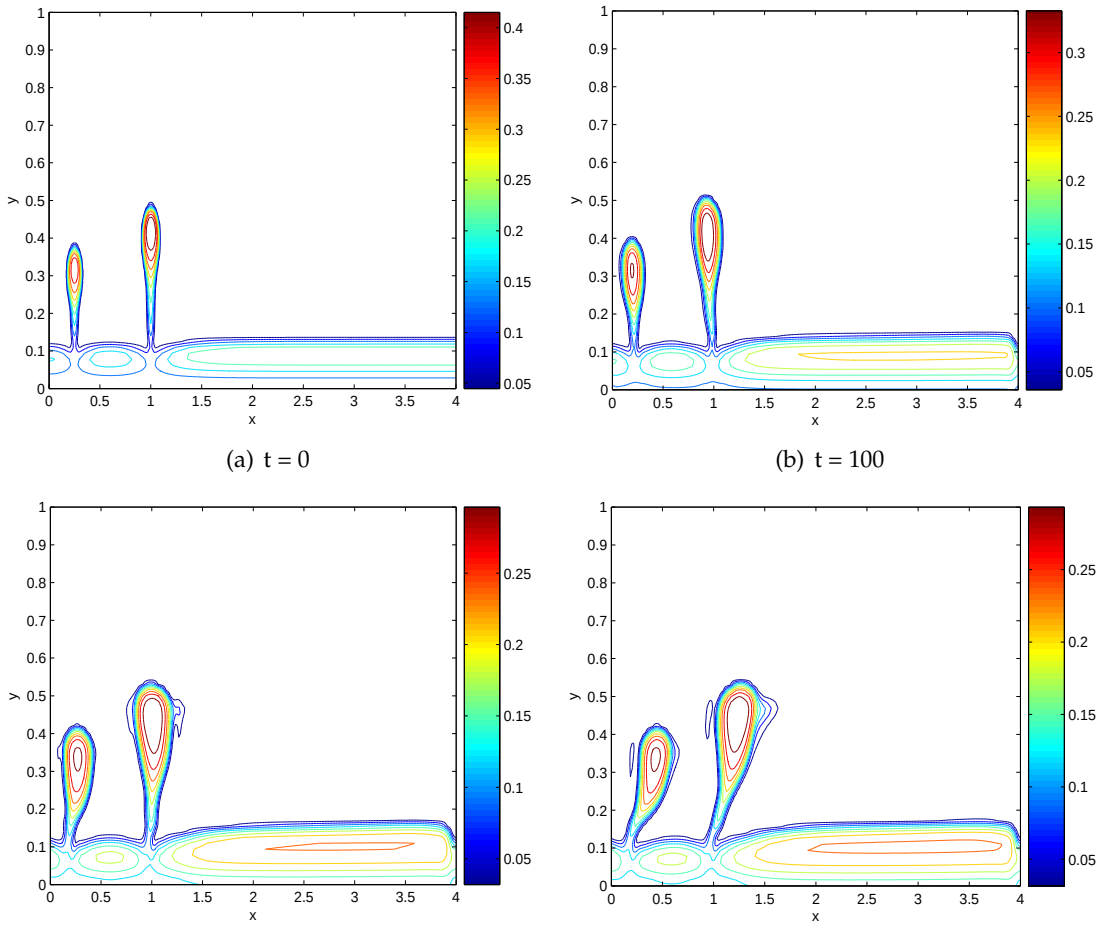

Figure 14: Oscillatory shear flow over two mushroom shaped humps with thin necks while the EPS production is considered. Some shedding effect is shown.

in the simulation. The period of the driving velocity is 100. We observe that the biofilm float to the right after half period of positive speed u ($t=50,250$), and then to the left after the other half period of negative u ($t=200,400$). Also, both humps detach from the base biofilm in the end. For oscillatory shear flows, it demonstrates that both humps of biofilms are equally easily to detach from the base. But for the shear flow with uniform speed at $y=1$, the hump upstream is prone to detach than the downstream hump.

Our simulations in weak shear demonstrate whether shedding or pinching-off occurs depends crucially on the initial profile of the biofilm as well as the driving speed of the shearing plate. If the biofilm-solvent interface has a smooth surface, then shedding is more easy to happen. On the other hand, if the biofilm-solvent interface has a rough surface or there are humps on a relative flat base connecting to the bulk by thin necks

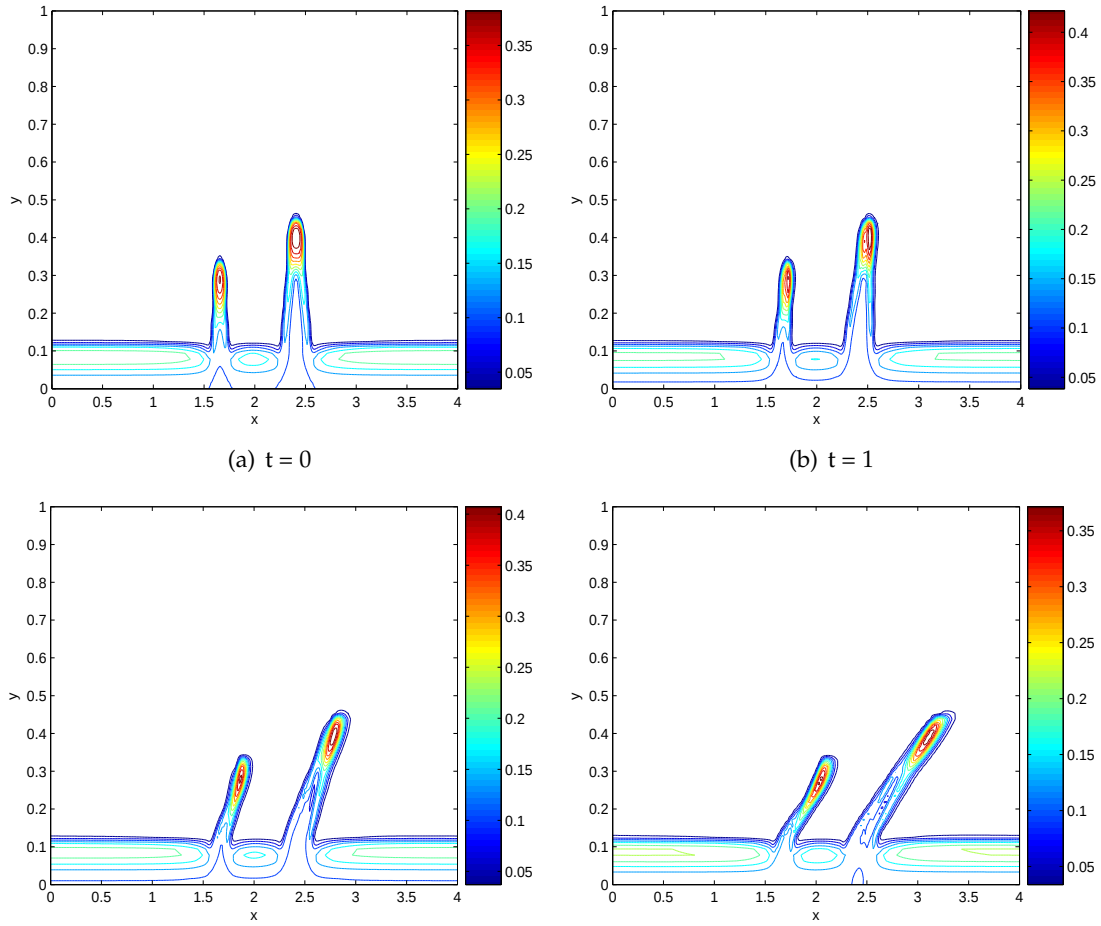

Figure 15: Shear flow over two mushroom shaped humps with thick necks in the middle of the domain while the EPS production is considered. The plate speed is $u=1000$. The two humps bend to the flow direction.

or bridges, then pinching-off (or detachment) is more likely to occur. Apparently, higher shear rate facilitates shedding and pinch-off to occur sooner.

Fig. 14 shows another oscillatory shear flow over two mushroom shaped humps on a flat base with thin necks. The moving plate velocity at $y=1$ is

$$u=0.1\sin(\frac{2\pi}{100}t), \quad v=0.$$

With the EPS production on, the simulation depicts a wobbling pair of mushroom shaped humps. They shed small pieces biofilm colonies during the wobbling motion. This is distinct from the case where the EPS production is turned off and the computational domain is shorter. Through the simulations conducted, one observes that both shedding and pinching-off occurs more easily in the square domain than in the long channel. For

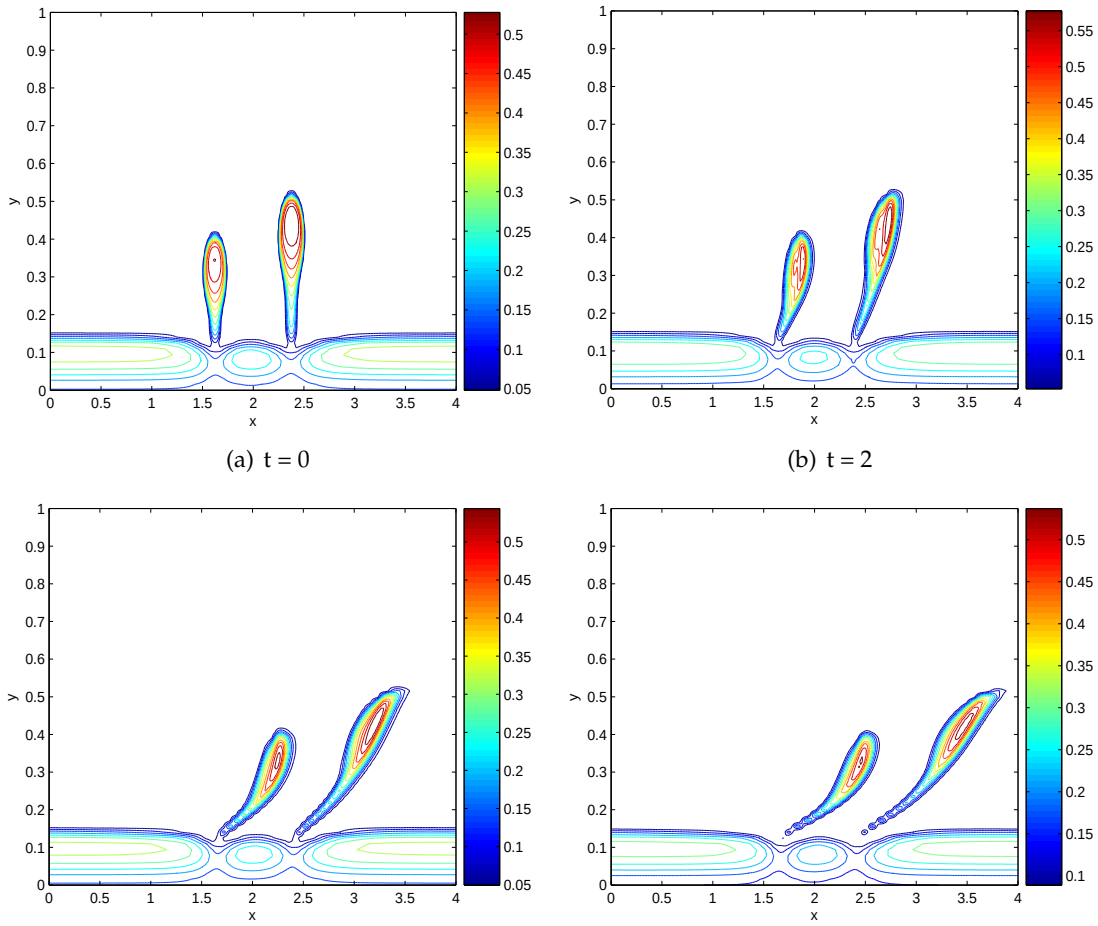

Figure 16: Shear flow over two mushroom shaped humps with thin necks while the EPS production is considered. The plate speed is $u=1000$. Both humps pinch off.

the square domain, the periodic boundary condition in x-direction may not be quite realistic for the oscillatory shear flow and it magnifies the impact of the shear flow on the biofilm, thus causes a stronger pinching-off effect. For the longer channel, on the other hand, in oscillatory shear flows, the u velocity component oscillates between positive and negative values and cancel each other's effect, thus it leads to a weaker pinching-off effect.

We next simulate dynamics of the biofilm in strong shear flows.

5.2.2 Dynamics in strong shear

We again use the growth time scale as the characteristic time in the nondimensionalization process. In a strong shear, the dimensionless plate driving speed is then large. In all

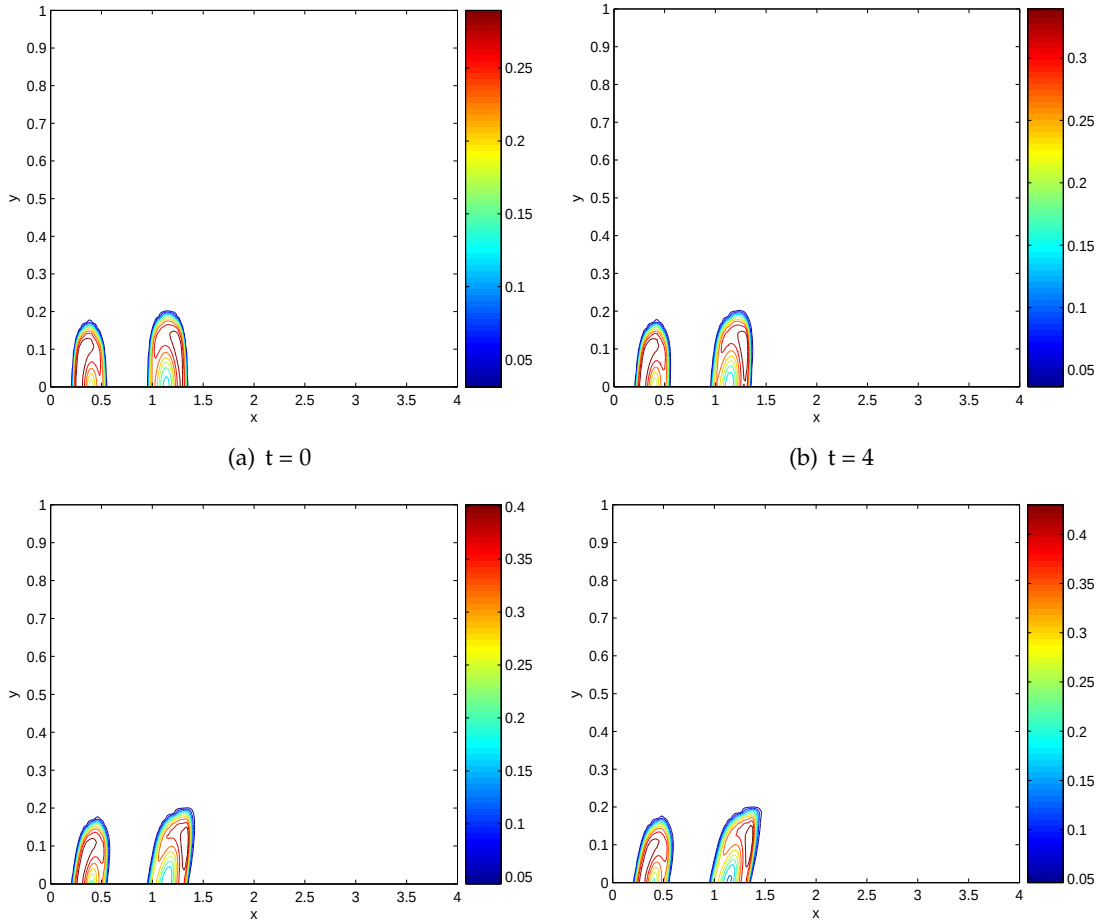

Figure 17: Shear flow over two humps with smooth interfaces while the EPS production is considered. The plate speed is $u=1000$. Slight bending is shown.

simulations presented below, the dimensionless speed is set at $u=1000$, the characteristic time scale $t_0=1000s$, and the viscosity for the polymer network is identical to the case used in the simulation in a cavity.

We first repeat the calculation with the similar initial data as in Fig. 8. Fig. 15 shows the simulation with the shear flow over two humps with thick necks in the middle of a flat base. The outcome is qualitatively the same as the one in the weak shear. The humps are bent toward the flow direction without detaching in the time period we simulated. Next, we examine humps with thin necks. Fig. 16 shows the shear flow over two humps at the middle of a flat base, where the necks are thin. Both humps quickly deform and detach from the base. These two cases are qualitatively the same as the corresponding ones in the weak shear flow, but the deformation and detachment takes place in much short time

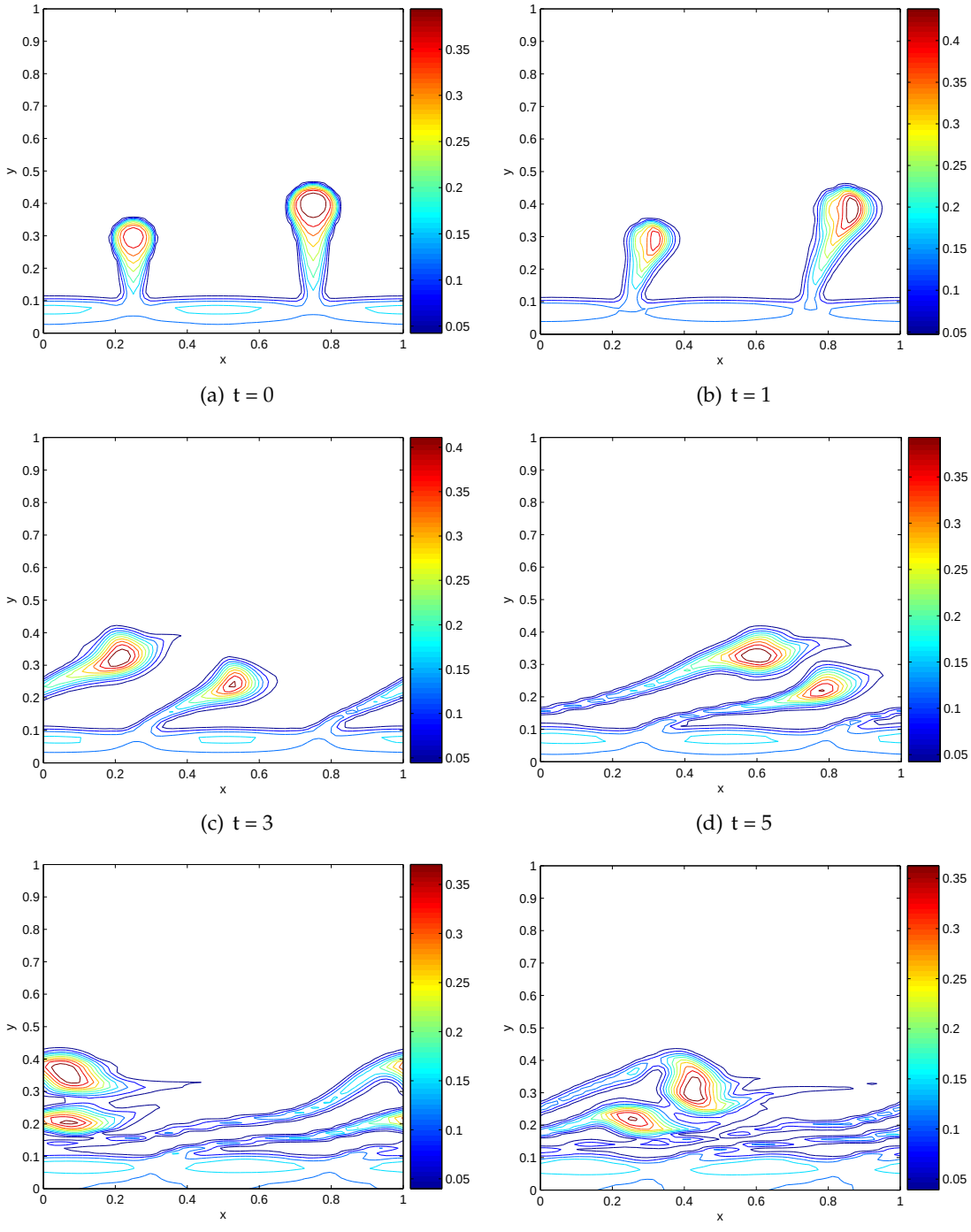

Figure 18: Shear flow over two mushroom shaped humps in a square domain while the EPS production is considered. The plate speed is $u=1000$. The humps deform severely without pinching off.

scales in the current situation. We remark that the humps in the weak shear case are set close to the left boundary in order to have longer flow biofilm interaction range within one period of the computational domain. We observe that a notch is developed in the bottom right of Fig. 8(d). We set the humps at the middle of the base in the strong shear case to ensure that periodic boundary conditions are being correctly implemented, and no notch is developed then.

Fig. 17 depicts the shear flow flowing over two sturdy humps with smooth interfaces rooted on the substrate. The observed shedding phenomena in weak shear is not observed in the time scale we simulate ($t = 10$). At even stronger shear, shedding can be observed though. However, the pinched-off pieces are convected quickly downstream. Fig. 18 shows the shear flow flowing over two mushrooms in a square domain. The detachment and merger of detached pieces does occur like in the previous case, but the elongated humps are stretched over the computational (periodic) domain.

The dynamics repeated in strong shear correlates with what we observed in the weak shear in long time with the reduced polymeric viscosity. In light of this, these numerical studies demonstrate the capability of the model and the numerical schemes for studying this complicated biological system. The phenomena simulated here correlate with what have been observed in experiments and natural settings qualitatively [6, 23].

6 Conclusion

We present some numerical simulations of the growth of biofilm colonies, their deformation, and detachment in a cavity and under plane shear using the extended Newtonian model we developed for biofilm and solvent mixtures recently [28]. Rippling of bumpy biofilm-solvent interfaces under shear, interface shedding of small pieces and pinching off of the large chunk of biofilms are observed in the simulations. The mechanism associated with shedding occurs when the extrusion or hump of biofilms into the solvent region connects to the bulk biofilm region through strong connections (thick necks or bridges); whereas, the detachment is observed only in the mushroomed islands connecting to the based biofilm colony by thin necks or bridges. The growth and coalesce of detached biofilm blobs are captured by our simulations. The EPS production is shown to stabilize or strengthen the biofilm and thereby reduces or delay the pinching off and/or shedding effect. These studies demonstrate the capability of the model and the numerical simulation tools associated with it. We look forward to seeing simulations in fully 3-D and more realistic geometries.

Acknowledgments

Effort sponsored by the Air Force Office of Scientific Research, Air Force Materials Command, USAF, under grant number F49550-05-1-0025 and the National Science Foundation through grants DMS-0605029 and DMS-0626180 are gratefully acknowledged. Finally, Qi

Wang and Tianyu Zhang would like to express their appreciation to the hospitality provided by the S. S. Chern Institute of Mathematics at Nankai University during their visit in the summer of 2007, where part of the work was completed.

References

[1] E. Alpkvist and I. Klapper, A Multidimensional Multispecies Continuum Model for Heterogeneous Biofilm Development, Preprint, 2005.
[2] A. N. Beris and B. Edwards, Thermodynamics of Flowing Systems, Oxford Science Publications, New York, 1994.
[3] R. B. Bird, R. C. Armstrong and O. Hassager, Dynamics of Polymeric Liquids, vol. 1 & 2, John Wiley and Sons, New York, 2987.
[4] J. W. Cahn and J. E. Hilliard, Free energy of a nonuniform system. I: Interfacial free energy, J. Chem. Phys., 28 (1958), 258-267.
[5] J. W. Cahn and J. E. Hilliard, Free energy of a nonuniform system. III. Nucleation in a two-component incompressible fluid, J. Chem. Phys., 31 (1959), 688-699.
[6] N. Cogan and J. Keener, The role of biofilm matrix in structural development, Math. Med. Biol., 21(2) (2004), 147-166.
[7] N. G. Cogan and J. Keener, Channel formation in gels, SIAM J. Appl. Math., 65(6) (2005), 1839-1854.
[8] B. Costerton, Medical Biofilm Microbiology: The Role of Microbial Biofilms in Disease, Chronic Infections, and Medical Device Failure, CD-ROM, Montana State University, 2003.
[9] J. Dockery and I. Klapper, Finger formation in biofilm layers, SIAM J. Appl. Math., 62 (2002), 853-869.
[10] M. Doi and S. F. Edwards, The Theory of Polymer Dynamics, Oxford Science Publications, Oxford, 1986.
[11] M. Doi, Introduction to Polymer Physics, Oxford Science Publications, Oxford, 1995.
[12] P. J. Flory, Principles of Polymer Chemistry, Cornell University Press, Ithaca, NY, 1953.
[13] J. L. Guermond, P. Minev and J. Shen, An overview of projection methods for incompressible flows, Comput. Method. Appl. Mech. Engrg., 195 (2006), 6011-6045.
[14] D. J. Hassett, P. A. Limbach, R. F. Hennigan, K. E. Klose, R. E. Hancock, M. D. Platt and D. F. Hunt, Bacterial biofilms of importance to medicine and bioterrorism: Proteomic techniques to identify novel vaccine components and drug targets, Expert Opin. Biol. Ther., 3(8) 2003, 1201-7.
[15] R. G. Larson, The Rheology of Complex Fluids, Oxford University Press, New York, 1998.
[16] C. A. A. Lima, R. Ribeiro, E. Foresti and M. Zaiat, Morphological Study of Biomass During the Start-Up Period of a Fixed-Bed Anaerobic Reactor Treating Domestic Sewage, Brazilian Archives of Biology and Technology.
[17] I. Klapper, Effect of heterogeneous structure in mechanically unstressed biofilms on overall growth, B. Math. Biol., 66 (2004), 809-824.
[18] I. Klapper, C. J. Rupp, R. Cargo, B. Purvedorj and P. Stoodley, Viscoelastic fluid description of bacterial biofilm material properties, Biotechnol. Bioeng., 80(3) (2002), 289-296.
[19] I. Klapper and J. Dockery, Role of cohesion in the material description of biofilms, Phys. Rev. E, 74 (2006), 031902.
[20] C. S. Laspidou and B. E. Rittmann, Modeling biofilm complexity by including active and inert biomass and extracelluar polymeric substances, Biofilm, 1 (2004), 285-291.

[21] S. T. Milner, Dynamical theory of concentration fluctuations in polymer solutions under shear, Phys. Rev. E, 48(5) 1993, 3674-3691.
[22] C. Picioreanu, M. van Loosdrecht and J. Heijnen, Mathematical modeling of biofilm structure with a hybrid differential-discrete cellular automaton approach, Biotechnol. Bioeng. 58 (1998), 101-116.
[23] C. Picioreanu, M. van Loosdrecht and J. Heijnen, Multidimensional modelling of biofilm structure, in: C. R. Bell, M. Brylinsky and P. Johnson-Green (Eds.), Biotech. Microbial Biosystems: New Frontiers, Proceedings of the 8th International Symposium on Microbial Ecology, Atlantic Canada Society for Microbial Ecology, Halifax, Canada, 1999.
[24] C. Picioreanu, M. J-U Kreft and M. van Loosdrecht, Particle-based multidimensional multispecies biofilm models, Appl. Environ. Microbiol., May (2004), 3024-3040.
[25] C. Picioreanu, J. B. Xavier and M. van Loosdrecht, Advances in mathematical modeling of biofilm structure, Biofilm, 1 (2004), 337-349.
[26] H. Tanaka, Viscoelastic model of phase separation, Phys. Rev. E, 56(4) (1997), 4451-4462.
[27] C. Wolgemuth, E. Hoiczyk, D. Kaiser and G. Oster, How myxobacteria glide, Curr. Biol., 12 (2002), 369-377.
[28] T. Zhang, N. Cogan and Q. Wang, Phase-Field Models for Biofilms. I. Theory and 1-D Simulations, submitted to SIAP, 2007.